Chip-Scale Angle-Selective Imager for *In Vivo* Microscopic Cancer Detection

Efthymios P. Papageorgiou, *Member, IEEE*, Bernhard E. Boser, *Fellow, IEEE*, and Mekhail Anwar, *Member, IEEE*

***Abstract*—We present an image sensor incorporating angle-selective gratings for resolution enhancement in contact imaging applications. Optical structures designed in the CMOS metal layers above each photodiode form the angle-selective gratings that limit the sensor angle of view to $\pm 18°$, rejecting background light and deblurring the image. The imager is based on a high-gain capacitive transimpedance amplifier pixel using a custom 11fF MOM capacitor, achieving 8.2 V $s^{-1}pW^{-1}$ sensitivity. The pixel includes a leakage current minimization circuit to remove signal-dependent reset switch leakage and the corresponding dark current is 14 $aA/\mu m^2$. The resulting 4.7 mm by 2.25 mm sensor (80 by 36 pixels) is designed specifically for intraoperative cancer imaging in order to solve the pervasive challenge of identifying microscopic residual cancer foci *in vivo*, where they can be removed. We demonstrate imaging and detection of foci containing less than 200 cancer cells labeled with fluorescent biomarkers in 50 ms with signal-to-noise ratios greater than 15 dB and the detection of microscopic residual tumor in mice models. The absence of large optical elements enables extreme miniaturization, allowing manipulation within a small, morphologically complex, tumor cavity.**

***Index Terms*—Angle-selective imaging, cancer detection, capacitive transimpedance amplifier (CTIA), fluorescence imaging, image sensor, sensor-on-a-chip.**

I. Introduction

MINIATURIZED optical imaging systems are critical for both consumer and medical applications. These systems are portable and are used in confined spaces that are not accessible using conventional imagers. Indeed, chip-scale solutions for contact imaging have enabled a variety of applications ranging from optical scanning and fingerprint sensing to lab-on-a-chip or implantable sensors used for medical disease research and diagnosis. Additional applications have been and will continue to be made possible by replacing many of the traditional large-scale optical elements, such as lenses, filters, and gratings, with on-chip structures fabricated in the metal layers of modern integrated circuit (IC) processes.

These on-chip optical techniques take advantage of the material properties and precise alignment of the CMOS metal interconnect and surrounding dielectric. Structures designed to enable 3D imaging [1], [2], polarization imaging [3], and optical wavelength filtering [4] have been previously described. However, one of the main attractions of CMOS image sensors is their planar form factor and ability to be scaled to any convenient surface area for contact imaging applications. Comparatively less work has been done to improve the resolution of these contact image sensors. We have developed on-chip optical structures called angle-selective gratings (ASGs) that restrict the angle of incident light allowed to enter the image sensor. The restricted angle-of-view provided by the ASGs not only allows higher resolution images to be obtained, but blocks out a large portion of background light in applications where signal and background levels are comparable, such as in intraoperative imaging.

More specifically, one of the high impact applications for chip-scale angle-selective contact imagers is the successful treatment of early stage cancers. This treatment requires the surgical removal of microscopic cancer foci from a background of 10^8 to 10^9 physically similar healthy cells. While the goal is often to remove all cancer cells, foci of 200 cancer cells or more represent a clinical threshold in breast cancer staging, worsening patient outcomes, and need to be removed [5]. Similar considerations apply to prostate cancer treatment. Consequently, physicians face a challenging tradeoff between removing excessive healthy tissue or risking leaving tumor behind. Modern techniques for identifying cancer cells use targeted biomarker labels for imaging under a high-magnification fluorescence microscope. However, the large size and rigidity of these microscopes limit them to line-of-sight imaging, making them ill-suited for imaging complex tumor cavities in minimally invasive surgeries [6]. Fiber optic-based imagers [7] are similarly hindered by fiber bending radius limitations. Existing compact alternatives do not have adequate resolution to detect microscopic cancer [8], [9]. Other chip-scale sensors requiring microfluidics or tissue samples need handling that is incompatible with the constraints of surgical procedures [4], [10], [11]. Some works, such as [10], have used fiber optic faceplates to reduce the angle of incident

Manuscript received August 17, 2019; revised October 20, 2019; accepted November 27, 2019. Date of publication December 12, 2019; date of current version February 4, 2020. This work was supported in part by the Department of Defense (PC141609), in part by the Mary Kay Ash Charitable Foundation (P0506430), in part by NIH/NCRR UCSF-CTSI Grant (UL1 TR000004), in part by the American Society of Clinical Oncology (4300-134078-44), in part by the Cancer League, and UCSF Cancer Center Give Breast Cancer the Boot, and in part by the National Science Foundation Graduate Research Fellowship Program. This paper was recommended by Associate Editor S. Ostadabbas. *(Corresponding author: Efthymios P. Papageorgiou.)*

E. P. Papageorgiou was with the Department of Electrical Engineering and Computer Sciences, University of California, Berkeley, CA 94720 USA. He is now with the Bosch Research and Technology Center, Sunnyvale, CA 94085 USA (e-mail: epp@eecs.berkeley.edu).

B. E. Boser is with the Department of Electrical Engineering and Computer Sciences, University of California, Berkeley, CA 94720 USA (e-mail: boser@eecs.berkeley.edu).

M. Anwar is with the Department of Radiation Oncology, University of California, San Francisco, CA 94158 USA (e-mail: mekhail.anwar@ucsf.edu).

Color versions of one or more of the figures in this article are available online at http://ieeexplore.ieee.org.

Digital Object Identifier 10.1109/TBCAS.2019.2959278

light allowed into the image sensor. However these fiber optic arrays are several millimeters thick, significantly increasing the size of the imaging system, require additional precision optical assembly steps after the CMOS fabrication in order to align it on top of the imaging area, and increase the overall cost of the imaging system.

We overcome these limitations by introducing a custom CMOS image sensor incorporating ASGs as we indicated above. The ASGs are embedded in the metal layers inherent to all CMOS processes, do not require additional assembly after fabrication, do not increase the thickness of the sensor, and do not increase the cost of the overall imaging system. We shrink the optics of conventional microscopes by orders-of-magnitude while retaining the ability to identify 200 tumor cells. The miniature size, high sensitivity, and low cost of our device facilitates its eventual integration into surgical tools, enabling real-time visualization of cancerous tissue without disrupting established surgical procedures.

This paper is organized into six sections. Section II details the angle-selective imaging operation and the design of the ASGs used in this work. Section III describes the presented angle-selective fluorescence contact imaging system and Section IV describes details of the pixel circuit design and operation. We present experimental results validating the sensor's ability to detect microscopic and residual cancer in Section V. The conclusion is provided in Section VI.

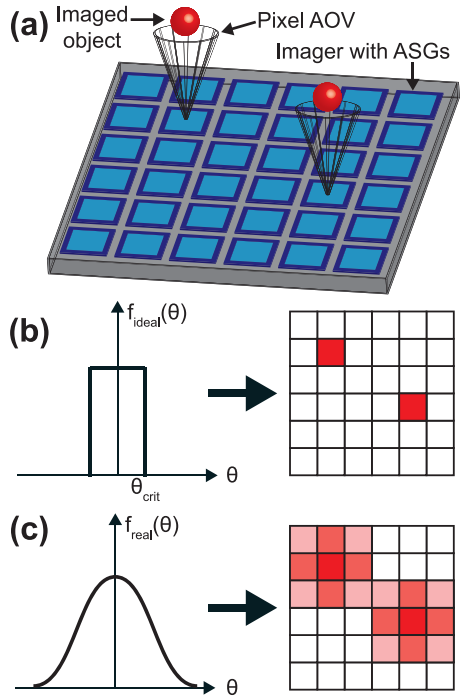

Fig. 1. (a) Angle-selective imaging operation. Each pixel has a restricted angle-of-view to enhance image resolution. (b) Ideal angle-selectivity function and captured image. (c) Realistic angle-selectivity function and captured image.

II. Angle-Selective Contact Imaging

The goal of angle-selective contact imaging is to replace large optical elements that limit miniaturization. A contact imager only produces a perfect image if the sample is placed directly on the imaging surface. Any distance between the sample and imager surface will allow light to diverge and blur the resulting image. Optical structures, ASGs, can be included within the pixels of the imaging chip to reject light that is not incident perpendicular to the surface of the chip and recover some of the resolution lost due to increased imaging distance. This procedure as well as the design of the ASG structure used in our image sensor is described in this section.

A. Angle-Selectivity Function

As illustrated in Fig. 1(a), each pixel in the imaging array accepts light from a limited angle of view (AOV) that is set by the ASGs. This AOV can be found from the angle-selectivity function, $f(\theta)$, of the gratings. The ideal angle-selectivity function, $f_{ideal}(\theta)$, would have a uniform response up to a specific angle, θ_{crit}, as shown in the left part of Fig. 1(b). Given knowledge about the size and shape of the objects to be imaged, θ_{crit} can be chosen such that in the resulting image all of the signal from the imaged object is contained in a single pixel, as illustrated in the right part of Fig. 1(b). Practical structures conforming to the design rules for CMOS metal interconnect do not have a perfect angle-selectivity function. As shown in Fig. 1(c), these structures have a more smoothly varying function, $f_{real}(\theta)$, and there will be some blurring between adjacent pixels in the captured image.

As long as the angle-selectivity function is well defined and the imaging distance is known, the point spread function (PSF) of the imaging system can be estimated accurately. A more selective angular response makes the estimate of the PSF insensitive to variation in the actual imaging distance, which is nominally set by a spacer placed over the surface of the sensor. The PSF is analogous to the impulse response of a dynamic system and can be used to predict the resulting image, $I(x, y)$, using:

$$I(x, y) = S(x, y) * PSF(x, y), \tag{1}$$

where $S(x, y)$ is the surface being imaged. The inverse operation can be performed to estimate the original surface using a variety of inverse filter and deconvolution algorithms. Details about this approach and results are presented in Section V-B.

B. ASG Structure

The ASG structure used in our image sensor is shown in Fig. 2 and is included in each sensor pixel. The motivation behind the design is to geometrically-limit the angles of light that are allowed to enter the pixel, improving the resulting image resolution (in order to detect smaller clusters of cancer cells) and improving the imagers robustness to variations in the imaging distance (which cannot be well controlled when using the sensor intraoperatively to detect cancer). The structure was designed to have the smallest apertures allowed by the design rules of the CMOS process, and thus the highest angle-selectivity, while covering as little of the photodiode area as possible to minimize insertion loss. Multiple metal layers are used to vertically increase the height of the structure, restricting

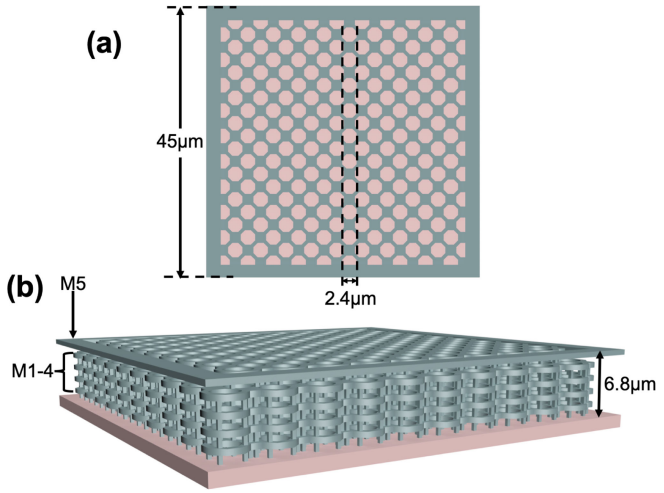

Fig. 2. (a) Top view of the ASG structure showing octagonally-packed array with 2.4 μm apertures. (b) Perspective side view of the 6.8 μm tall ASG structure in metal layers 1–5.

the angles of light allowed to enter the pixel, and thus increasing the angle-selectivity.

As shown in the top view in Fig. 2(a), each ASG consists of a 45 μm by 45 μm octagonally packed array with 2.4 μm apertures. The horizontal periodicity serves to completely cover the photodiode area. The perspective side view of the ASGs is shown in Fig. 2(b). The structure is designed in metal layers 1–5 and is encased in the inter-level dielectric (oxide). All of the metal layers are electrically connected together using vias. Metal layer 6 (the top metal layer) was not used as no chemical mechanical planarization is performed on the IC surface after its deposition. Including metal layer 6 would lead to an unpredictable and uneven surface that affects the performance of the ASGs by changing the incident angle of light. The entire structure is 6.8 μm tall. The insertion loss is 3.5 dB and is determined at normal incidence and by the amount of photodiode area covered by the ASGs, approximately 55%. The apertures when viewed at normal incidence are large, 2.4 μm, compared to the wavelength in the oxide layer (approximately 500 nm) of the emitted light we are trying to detect and thus diffraction effects are negligible. The angle-selectivity function described in the previous section quantifies the ASG's response relative to normal incidence and takes into account effects such as scattering and reflection off the sides of the metal layers. These effects will be further discussed in the next section. The insertion loss and angle-selectivity function together describe the transmittance of the ASGs. This grating structure is natively manufactured in a conventional 0.18 μm CMOS process and does not require any additional fabrication or deposition steps.

C. Angle-Selectivity Simulation and Measurement

The ASG structure was designed and simulated using the finite element method (FEM) in COMSOL. The COMSOL simulations are needed in order to account for side reflection and interference effects in the 3D grating structure which cannot be accounted for using simple geometric optic estimation methods alone. These simulations were conducted for 720 nm wavelength light, close to the wavelength of light emitted by NIR fluorophores used for *in vivo* imaging. The structure was optimized to provide a sharp angle-selectivity function without an excessively large insertion loss and while keeping to the design rules provided in the used 0.18 μm technology. The simulated field plot of the ASGs for varying incident angle is shown in Fig. 3. Periodic boundary conditions were used to reduce the simulation size. Thus only the simulation of a single element in the ASG array is shown. Light is incident from the top side of the structure and the detector (photodiode) is placed at the bottom. As the incident angle is increased, less light is allowed to pass through the ASG and more light is reflected out of the structure. Hence, for each angle, a certain portion of the light reaches the photodiode.

The simulated transmittance of the ASGs versus incident angle compiled from the FEM simulations is shown in Fig. 4 in blue. In the same plot we show the measured response of the ASGs from the fabricated image sensor in red. The two results are in close agreement and the difference between the two is likely due to the imperfect fabrication of the metal structures in the CMOS process (i.e. the fabricated metal wires do not have perfectly sharp edges or corners). The response of the photodiode covered with ASGs decreases to 50% at approximately 18°, a full width at half maximum (FWHM) of 36°. Also shown in Fig. 4 is the simulated response of an image sensor that does not incorporate ASGs. This response is a cosine function with a FWHM of 120°, due to the effective reduction in imaging area as incident angle increases. The reduced FWHM of the response of the photodiode with ASGs allows it to obtain a higher imaging resolution and block a large portion of background light.

III. Sensor for Intraoperative Fluorescence Imaging

Image sensors incorporating ASGs can be used in a variety of applications, including intraoperative cancer imaging. This section presents details on fluorescence imaging in general, the system architecture for our angle-selective contact fluorescence imager, and a method to calculate expected fluorescence signal levels.

A. Fluorescence Imaging

We are performing fluorescence imaging as illustrated in Fig. 5(a). The tumor cells are labeled with a fluorescent probe. This probe consists of a fluorophore conjugated with an antibody that specifically targets and binds to tumor cells. This fluorescent probe can be injected into the patient several hours or days before an operation is performed in order to allow time for the binding to occur [12], [13]. Excitation light (from a laser, shown in blue) is used to excite the fluorophores, causing them to emit at a higher wavelength (shown in red). The emitted light is selected by an optical filter and is then detected by a sensor (photodiode).

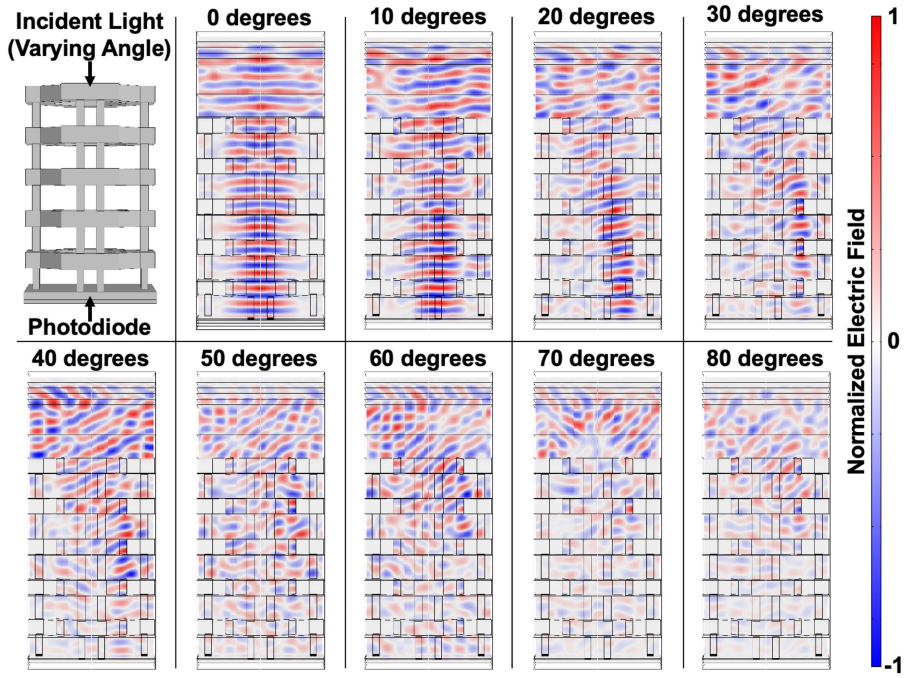

Fig. 3. ASG 3D FEM simulation for varying incident angle showing increased attenuation for steeper angles. Periodic boundary conditions are used and only a single element in the octagonally-packed array is simulated.

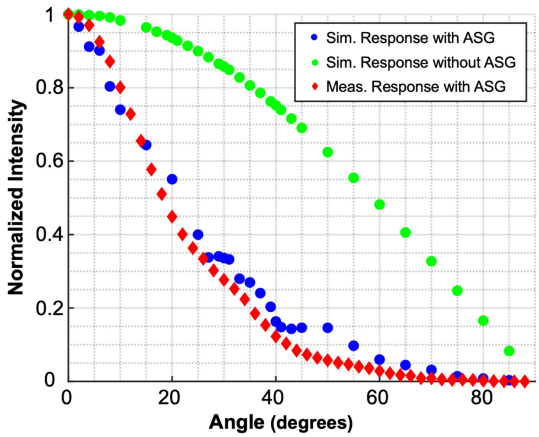

Fig. 4. Simulated (Sim. in blue) and measured (Meas. in red) ASG response versus input angle showing good agreement. The simulated response of an uncovered photodiode without ASGs (green) is also shown.

B. Angle-Selective Contact Fluorescence Imaging System

A diagram of our chip-scale angle-selective fluorescence contact imager is shown in Fig. 5(b). The excitation light can be provided by a linear fiber optic array, collimated light source, or, for a fully-integrated solution, by laser diodes arrayed around the imaging chip. A small gap is needed between the image sensor and the surface containing the labeled cancer tissue in order to apply the excitation light. This gap is provided by a 500 μm thickness fused silica spacer as shown. The minimum spacing is close to 500 μm for an imager with one dimension equal to 2.25 mm. The total internal reflection critical angle of the fused silica-tissue interface limits this spacing from being reduced further.

The optical filter is a layer on the order of 10 μm thick that allows the fluorescence emission light (shown in red) to pass through, but blocks the excitation light. We are using an amorphous silicon absorption filter as described in [14] in order to block the excitation light while maintaining a small form factor. The filter relies on absorption and material properties of amorphous silicon and rejects excitation light at all incident angles. Conversely, thin-film interference filters commonly used for fluorescence imaging have a strong angular dependence and their rejection falls off for oblique incident light angles. This makes the conventional filters not suitable for intraoperative contact imaging where excitation light needs to illuminate highly-scattering tissue at steep angles. The filter is epoxied to the angle-selective imaging chip using a clear optical epoxy. The imaging chip is used to detect the fluorescence and consists of an array of photodiodes covered by the ASGs as described in the previous section.

The block diagram of the imaging chip is shown in Fig. 6. The chip consists of an 80 (horizontal) by 36 (vertical) array of pixels. Each pixel contains a photodiode covered by an angle-selective grating. The details of the pixel architecture will be explained in Section IV. This is a global shutter image sensor and the pixels are read out row-wise onto shared pseudo-differential column lines. The rows are read sequentially and selected by digital row driving circuitry shown on the right. The 80 differential column lines are multiplexed to eight output lines that are digitized using off-chip ADCs. An FPGA reads the data from the ADCs, performs the digital programming and control of the

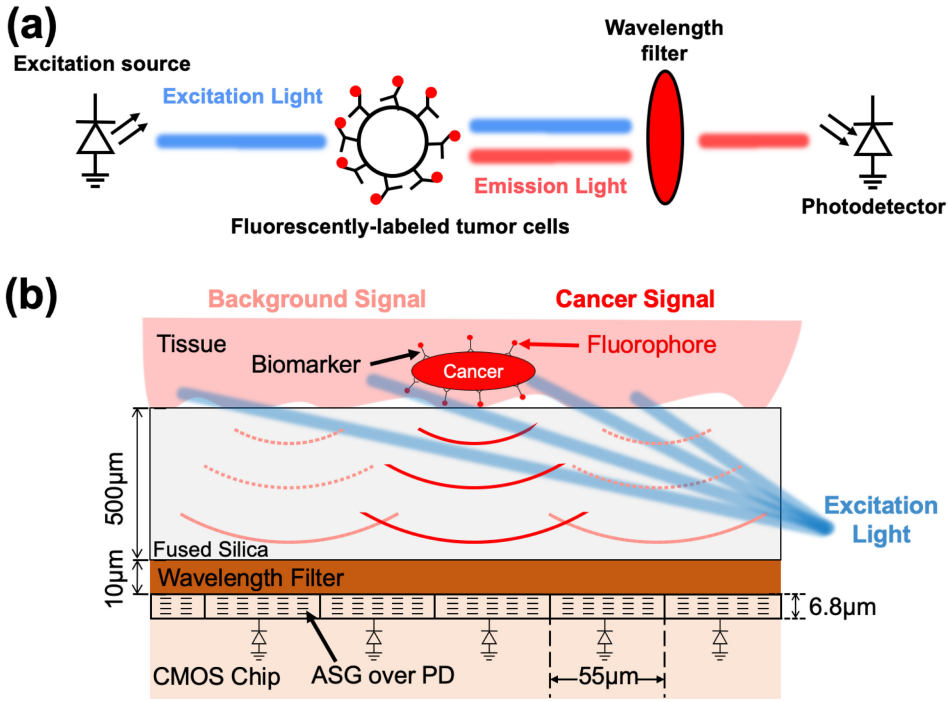

Fig. 5. (a) Fluorescence imaging operation. (b) Angle-selective contact fluorescence imaging system including labeled cancer tissue, excitation light, optical wavelength filter, and angle-selective imaging chip.

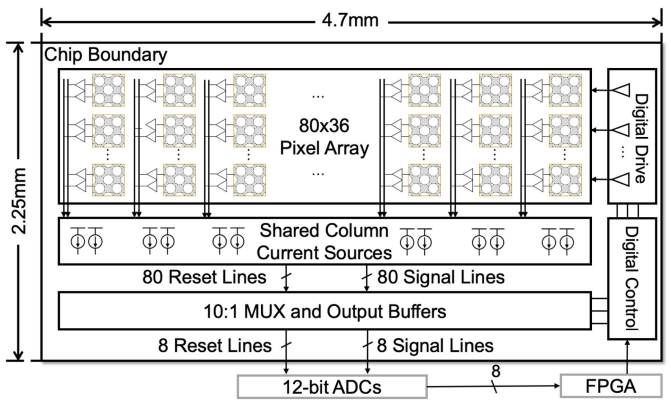

Fig. 6. Imaging chip block diagram showing 80 by 36 pixel array. The array is read out row-wise on to shared column lines.

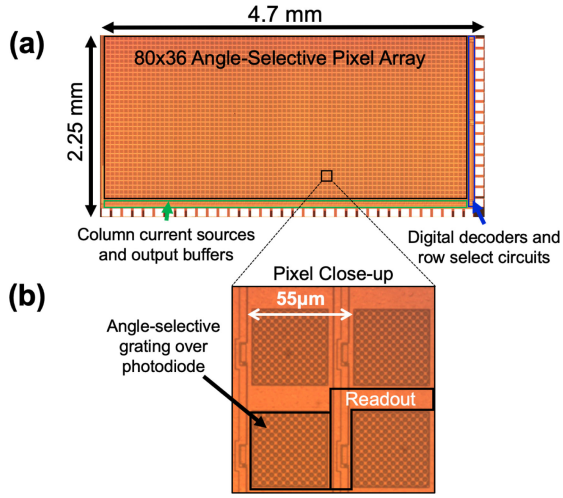

Fig. 7. (a) Die microphotograph showing imaging array, analog circuitry along the bottom side, and digital circuitry along the right. The chip is 4.7 mm by 2.25 mm and the array is 4.4 mm by 1.98 mm. (b) The inset shows pixels with 55 μm pitch and the ASGs over the 44 μm by 44 μm photodiodes.

chip, and communicates with a PC for real-time data capture and visualization.

The microphotograph of the image sensor appears in Fig. 7(a). The sensor is 4.7 mm by 2.25 mm and most of the area (4.4 mm by 1.98 mm) is taken up by the imaging array. The analog column current sources, multiplexers, and buffers are along the bottom row of the array. The digital decoders and row driving circuitry are along the right side. An inset showing a close-up image of four pixels is shown in Fig. 7(b). The ASGs are visible above each photodiode. The pixel pitch is 55 μm. Each photodiode has dimensions 44 μm on a side and the pixel readout circuitry is placed in the surrounding 11 μm channels. The overall fill factor of each pixel is 28%, accounting for the area covered up by the ASGs.

C. *Fluorescence Signal*

The fluorescence signal received from a single cell or a focus of cells can be estimated using information about the cell and antibody binding properties, as well as the imaging distance and imager sensitivity. The signal from a single cell, F (in W), can

be expressed as:

$$F = \sigma_{fl} Q_{fl} P_{in} N_{fl}, \tag{2}$$

where σ_{fl} is the fluorophore absorption cross section in cm^2, Q_{fl} is the fluorescence quantum yield, P_{in} is the incident light flux in W/cm^2, and N_{fl} is the number of fluorophores bound to the cell. A typical fluorophore that emits in the near-infrared, such as IR700DX, has a quantum yield and absorption cross section of approximately 10–30% and 10^{-16} cm^2, respectively [15]–[17]. A single cell can bind on the order of one million fluorophores when using a targeted antibody such as Trastuzumab for a corresponding HER2+ breast cancer. Typical excitation powers are close to 100 mW/cm^2.

In order to calculate the received signal during contact imaging from a focus of cancer containing N_{cell} cells, we need to incorporate the fluorophore emission profile, the pixel area (A_{pixel}), and the pixel response. Fluorophores uniformly emit radially in all directions, spreading the emitted power over a surface area of $4\pi z_{dist}^2$, where z_{dist} is the imaging distance. The power incident on a single pixel can thus be expressed as:

$$P_{incident} = F \cdot N_{cell} \cdot \frac{A_{pixel}}{4\pi z_{dist}^2}. \tag{3}$$

For the typical values given above, an imaging distance of 650 μm, and a pixel area of 44 μm^2, 200 cancer cells will provide a signal of close to 150 fW (using 20% for Q_{fl}).

The power that is actually received and the current generated in the photodiode will additionally depend on the angle-selectivity function, the insertion loss, L, due to the presence of the angle-selective gratings, and the responsivity, R, of the pixel. The angle-selectivity function is approximately equal to one when considering the pixel directly opposite a cancer cell focus, but needs to be accounted for when computing the background light received by a pixel (which arrives from all angles). The responsivity expresses how efficiently a photodiode or pixel converts incoming light power into the measured output signal, which may be a current or the output voltage. Accounting for all of these parameters, the final output signal is:

$$Signal = F \cdot N_{cell} \cdot \frac{A_{pixel}}{4\pi z_{dist}^2} \cdot f(\theta) \cdot (1 - L) \cdot R. \tag{4}$$

It is critical to maximize the pixel responsivity considering the small signal provided by even 200 cancer cells.

IV. Pixel Design

There are a number of challenges associated with ultrasensitive optical detection including signal-dependent dark current, signal-dependent gain and in-pixel offsets. The pixel circuit has been designed to eliminate these error sources in order to avoid extraneous calibration steps that affect the ease of use of the sensor. A custom metal-oxide-metal (MOM) integration capacitor and high gain amplifier is used to ensure a linear pixel response. A leakage current minimization circuit is used to remove signal-dependent reset switch leakage and correlated double sampling (CDS) circuitry suppress offset and noise. The design and operation of the pixel circuit and these elements are discussed in this section.

A. Pixel Operation and Timing

Fig. 8(a) shows the architecture of the pixel. This is a customized capacitive transimpedance amplifier (CTIA) architecture that was chosen for its high linearity and accurate gain while maintaining shot noise limited performance. The pixel contains the angle-selective photodiode, an integration capacitor, C_{int}, an amplifier (Amp), a reset switch, two sample-and-hold capacitors, and two source follower (SF) output buffers for readout on the column lines. The timing diagram for the pixel circuit appears in Fig. 8(b). Initially Φ_{RST} is high for a time t_{RST} (typically 100 μs) and the reset switch is closed, draining the charge across C_{int}. The signals Φ_R and Φ_S are also high, connecting the load capacitors C_{LR} and C_{LS} to the output of the amplifier. Φ_R goes low a time t_{wait} (100 μs) after Φ_{RST} falls, allowing time for the amplifier to settle, and the initial output value of the amplifier is stored on C_{LR}. After a further time, T_{int}, the integration time of the amplifier (generally 10 ms to 50 ms), Φ_S goes low, storing a value on C_{LS}. The difference between the two values is the output voltage of the pixel and is read onto the columns when the row select signal, Φ_{SEL}, rises during the imaging array readout. The resulting pixel output, V_{out} is

$$V_{out} = \frac{I_{in} \cdot T_{int}}{C_{int}}, \tag{5}$$

where I_{in} is the photocurrent generated in the integration capacitor by the input light. Details of the design of this pixel circuit are presented below.

B. Pixel Amplifier

The detailed pixel schematic appears in Fig. 8(c). The in-pixel amplifier consists of transistors M_1–M_4 configured in a cascoded common source configuration. The bias voltages V_{b1}–V_{b3} are provided through current mirrors placed outside the pixel array and are common to every pixel in the array. The nominal bias current is 50 nA. This current needs to be high enough to maintain the amplifier gain while charging the load capacitance for the maximum possible input signal level ($\sim$1 pA). The bias current should also be chosen large enough for fast dynamic settling during reset. However, we seek to minimize power consumption as much as possible and so a nominal bias of 50 nA was selected. The integration capacitor is connected between the gate of M_1 and the drains of M_2 and M_3. The sampling switches are full transmission gates consisting of pairs (M_{12}, M_{13}) and (M_{14}, M_{15}). The sample-and-hold capacitance is provided by a pair of MOS capacitors, C_{LS} and C_{LR} that have a nominal value of 150 fF, however, the actual value of these sample-and-hold capacitances depends significantly on the gate voltage level. This voltage-dependency does not affect the operation of the amplifier significantly, but must be accounted for in the noise calculations as described in Section IV-D. The reset switch and replica amplifier, used to drain the charge stored on C_{int} after integration and readout are completed, consists of transistors M_5–M_{11} and are described in more detail in the next section.

An advantage of the chosen CTIA architecture is that the amplifier gain is set by the value of the integration capacitor, C_{int}, rather than the variable and non-linear photodiode capacitance.

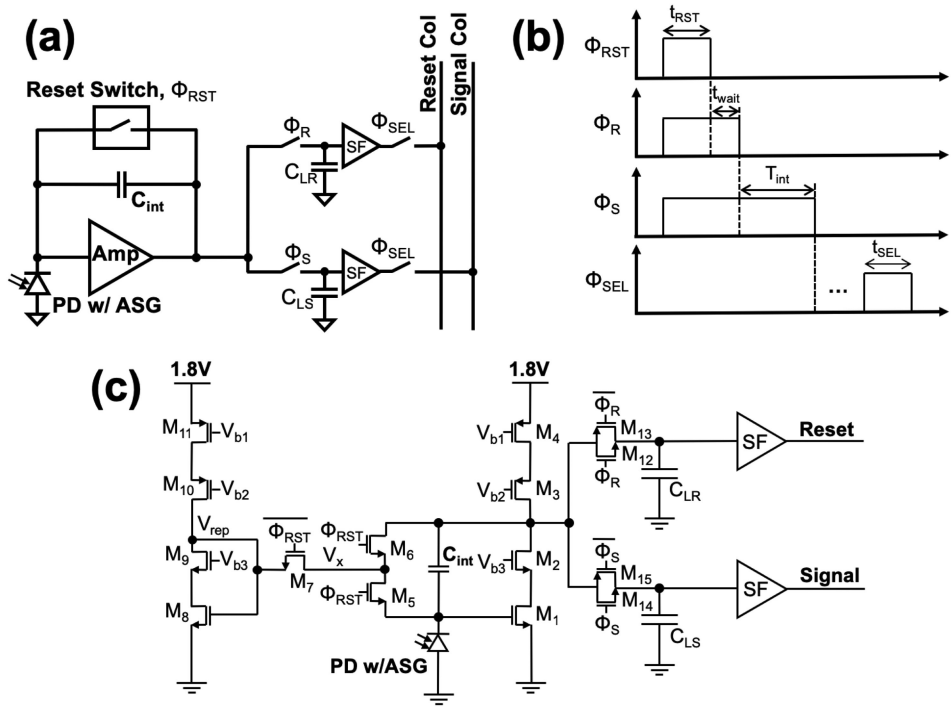

Fig. 8. (a) General pixel architecture showing photodiode, amplifier, integration capacitor, reset switch, sampling capacitors, and output source follower buffers. (b) Pixel timing diagram. (c) Detailed CTIA pixel schematic showing cascoded common source amplifier implementation and replica reset amplifier for leakage current minimization.

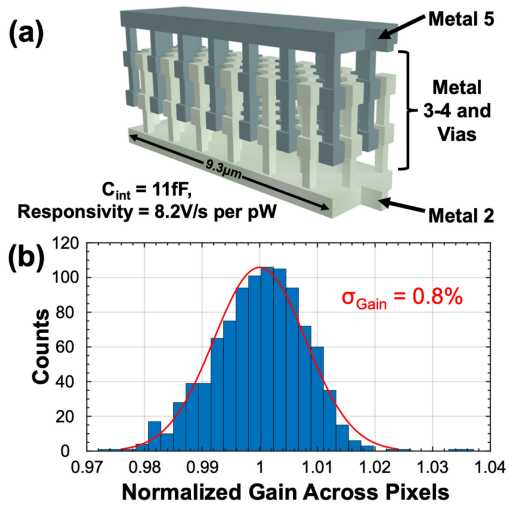

Fig. 9. (a) Lateral flux MOM capacitor 3D structure. (b) Measured normalized gain histogram across the chip showing 0.8% standard deviation.

This capacitor can be designed as a MOM or metal-intrinsic-metal (MIM) capacitor such that its value is independent of the input signal. For this amplifier, we have designed the lateral flux MOM integration capacitor shown in Fig. 9(a) with a value of 11 fF, significantly smaller than the 350 fF photodiode capacitance, allowing for a 30 dB higher voltage gain in the pixel. The resulting sensitivity of the pixel is 8.2 $\mathrm{Vs}^{-1}\mathrm{pW}^{-1}$ of incident light power. The capacitor is designed in metal layers 2–5 and has dimensions 9.3 μm by 2.7 μm. Some additional area in the pixel is required for this capacitor, but it is not significant compared to the large 44 μm by 44 μm photodiode.

The MIM capacitors in this technology exhibit worse matching (due to imprecise vertical control of the metal spacing) than the chosen lateral flux MOM topology. Mismatch between the gains of different pixels across the array is directly proportionate to the mismatch between the integration capacitors, as well as mismatch in the responses of the photodiodes. We have measured the gain response across the pixels in the array by applying a uniform, collimated, light on the surface of the image sensor and the resulting normalized gain histogram is plotted in Fig. 9(b) with a fit to a normal distribution shown in red. The standard deviation is 0.8%. For typical signal levels up to approximately 550 mV output voltage, the gain error will be below the noise of the pixel, and no gain calibration is necessary.

The total power consumption of the entire pixel array is approximately 500 μW. There is an additional 3 mW consumption from the column current sources and output buffers during readout (taking 1.1 ms for the entire array). However, this power can be reduced by turning off these elements while integrating the input light signal.

C. Leakage Current Minimization

Leakage and dark current present a serious challenge when trying to image small fluorescence signals. These currents effectively reduce the dynamic range available for imaging, increase the shot noise level, and cause offset and fixed-pattern noise

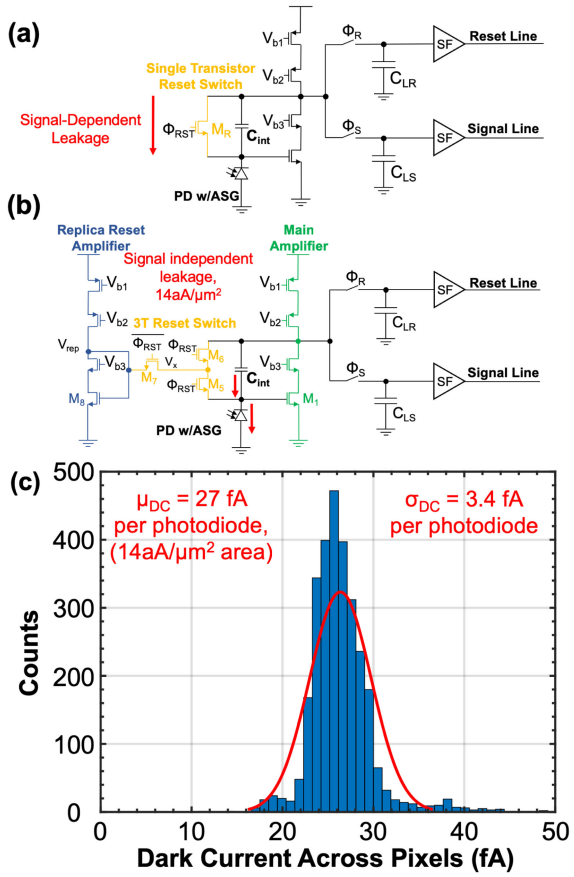

Fig. 10. (a) A conventional single-transistor reset switch has signal-dependent leakage. (b) The three-transistor reset switch and replica reset amplifier limit the voltage across the reset switch M_5, minimizing leakage current. (c) Histogram of measured dark current across the chip showing 27 fA mean and 3.4 fA standard deviation.

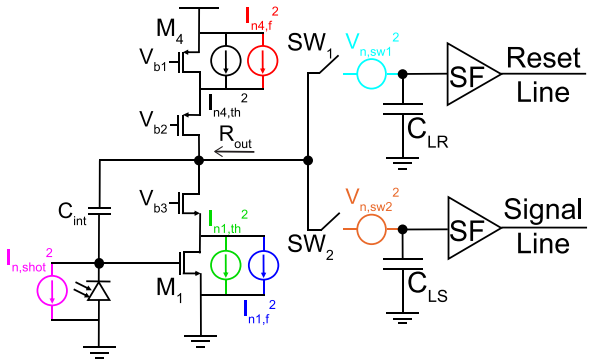

Fig. 11. Pixel schematic showing thermal, flicker, shot, and switch resistor noise sources.

to appear in the resulting images. However, if the fluorescence excitation light can be turned off, the dark current itself can be easily canceled at the beginning of the imaging process by taking several dark frames to obtain a pixel-by-pixel estimate of its value. This dark current image can be automatically subtracted in hardware or software from the images taken during the fluorescence imaging procedure. This operation removes the offset and fixed-pattern noise introduced by the dark current, but the shot noise due to its presence will not be canceled and the dynamic range will still be reduced. Additionally, the effect of leakage current will not be reduced by this operation and must be prevented using another method as described in this section.

Conventionally, a single reset switch is used to drain the charge on C_{int} during reset as shown in Fig. 10(a). In this configuration, when the transistor M_R is off during integration, the leakage current will be dependent on the voltage across it, which will in turn depend on the input signal level. This signal-dependent leakage requires complex calibration for each image. In order to avoid this, we have used the topology presented in Fig. 10(b). A three transistor reset switch consisting of M_5, M_6, and M_7 is used. The charge across C_{int} is drained through M_5 and M_6 during reset. During signal integration, these two devices are open and M_7 is closed, connecting the replica reset amplifier and the voltage V_{rep} to V_x. The replica reset amplifier is a duplicate of the main amplifier branch with the same 50 nA bias current. This operation limits the voltage across M_5 to approximately the mismatch voltage between M_1 and M_8, which is on the order of several mV and is signal independent. The leakage current is effectively eliminated and only the signal-independent dark current (the effect of which can be reduced using the method described above) remains in the pixel. A histogram of the dark current is shown in Fig. 10(c) measured at room temperature along with a fit to a normal distribution shown in red. Amplifier offsets have been subtracted using zero integration time calibration images and this histogram represents only the dark current. The mean dark current in each pixel is 27 fA, 14 aA/μm^2 of photodiode area, and the standard deviation is 3.4 fA.

D. Noise

The small integration capacitor and the resulting high gain of the pixel ensures that noise sources other than the pixel noise are negligible even for small fluorescence signals. The main noise sources in the pixel amplifier are shown in Fig. 11 and include M_1 and M'$_4$s thermal and flicker noise, the photodiode shot noise, and the noise from the two sampling switches SW_1 and SW_2. CDS is used in this pixel to cancel the intrinsic amplifier offsets and helps to suppress the amplifier noise. Two samples are taken during each integration cycle, one at the beginning of integration and one at the end. In general, the noise transfer functions for the same noise source will not be the same at these two different time points. In this amplifier, the loading capacitance changes between these two time points, as the value of the MOS capacitors C_{LR} and C_{LS} depends on the sampled signal level and additionally one of the load capacitors is disconnected to take the first sample (the reset level sample). The noise transfer functions for each noise component can thus be expressed in the general form as

$$H_n(s) = H_2(s)e^{-s \cdot T_{int}} - H_1(s), \tag{6}$$

where $H_1(s)$ and $H_2(s)$ are the transfer functions at the beginning of integration (right before SW_1 is disconnected) and end of integration (right before SW_2 is disconnected), respectively.

The thermal and flicker noise components all see the same transfer functions. Assuming the switch resistance values are chosen low enough to not interfere with the settling operation of the amplifier, this transfer function can be expressed as

$$H_{n,th,fl,1(2)}(s) = \frac{R_{out}}{1 + sR_{out}C_{Ltot,1(2)}}, \tag{7}$$

where R_{out} is the output resistance of the cascoded common source with C_{int} connected in feedback, $C_{Ltot,1}$ is the total load capacitance right before the reset sample is taken, and $C_{Ltot,2}$ is the total load capacitance at the end of the integration cycle before the second sample is taken. Note that this transfer function represents the transimpedance from a thermal noise or flicker noise current to the output voltage. The output resistance of the cascoded common source is very large, so $R_{out} = \frac{1}{F \cdot g_{mn}}$, where F is the feedback factor of the amplifier and g_{mn} is the transconductance of the transistor M_1. The feedback factor is defined as $F = \frac{C_{int}}{C_{int}+C_{PD}}$, where C_{PD} is the photodiode capacitance. The two load capacitances are $C_{Ltot,1} = C_{LR} + C_{LS} + C_{int}(1-F) = 2C_L + C_{int}(1-F)$ and $C_{Ltot,2} = C_{LS} + C_{int}(1-F) = C_L + C_{int}(1-F)$, where $C_{LR} = C_{LS} = C_L$.

The shot noise is integrated on C_{int} along with the input signal and has the same transfer function as the input signal. This transfer function can be expressed as

$$H_{n,sh,1(2)}(s) = \frac{\frac{g_{mn}}{sC_{int}} - 1}{\left[s\left(C_{PD} + C_{L,1(2)} + \frac{C_{PD}C_{L,1(2)}}{C_{int}}\right) + g_{mn} \right]}, \tag{8}$$

where $C_{L,1} = 2C_L$ and $C_{L,2} = C_L$. Note that the shot noise density is input dependent and expressed as a current ($i^2_{n,shot} = 2qI_D\Delta f$, where I_D is the total diode current), so this transfer function represents a transimpedance once again.

In the above equations, the load capacitors C_{LR} and C_{LS} are MOS capacitors and their capacitance may change throughout the integration, depending on input signal level. This varying capacitance must be accounted for and these terms can more generally be written in the form $C_L(V_L)$. This effect is significant in this design, with the initial value of the MOS capacitors being 65 fF at the reset voltage (0.53 V) and increasing up to 200 fF at 1.5 V.

The noise from the resistance of the sampling switches SW_1 and SW_2 is negligible for typical circuit component values, but the corresponding noise transfer function equations are included in the Appendix along with an explanation on how to find the expanded equations for thermal, flicker, and shot noise that account for the switch resistance.

The RMS noise contribution for each of the noise sources described above versus integration time is plotted in Fig. 12(a) for an input photogenerated current approximately equal to the average pixel dark current. Even for this smallest input current, the shot noise is the most significant noise source for the largest integration times, when the dynamic range of the pixel is being completely utilized. Fig. 12(b) depicts the total RMS noise in the amplifier versus integration time, showing both the calculated value (in blue) and the measured value from the ASIC (in red).

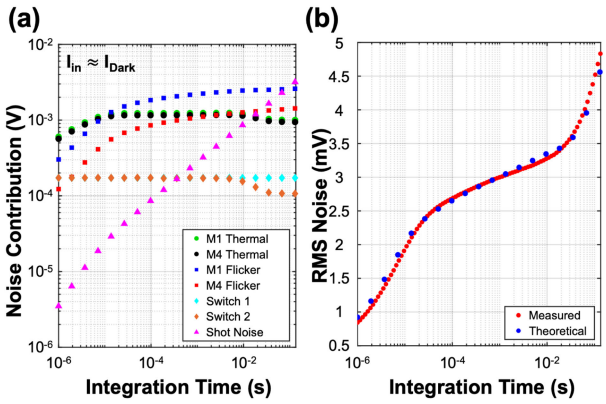

Fig. 12. (a) Theoretical RMS noise contributions for various noise sources versus integration time for a small input current value close to the dark current. (b) Measured (red) and theoretical (blue) total RMS noise versus integration time showing good agreement.

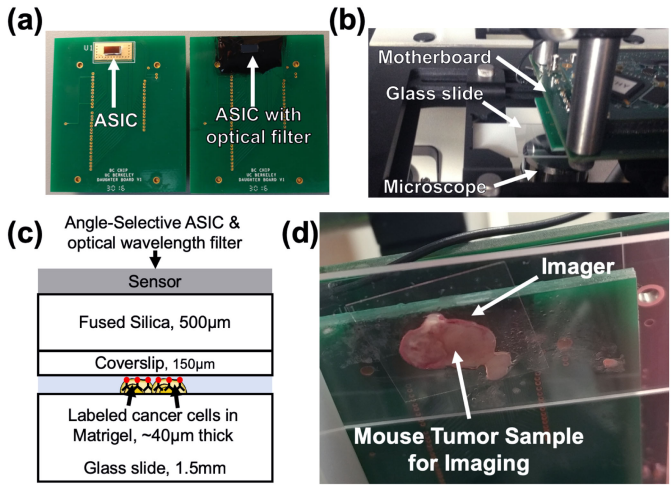

Fig. 13. (a) Imaging ASIC on PCB both without (left) and with (right) an optical filter. Dark epoxy is used for electrical isolation. (b) Imaging setup for 3D cell culture and tissue samples. The imaging ASIC is suspended over an inverted fluorescence microscope with a glass slide in between. (c) Diagram of imaging system. (d) Bottom view of imaging setup for larger tissue samples.

The calculated and measured values are in close agreement. For typical signal levels and integration times, the RMS noise will be close to 4.5 mV.

V. Cell and Tissue Imaging Results

This section describes imaging of a variety of samples, including 3D cell cultures and mouse tissue. The 3D cell culture results are used to characterize the imager's sensitivity to cancer cell foci with a wide range of sizes. The tissue results demonstrate the imager's ability to detect residual cancer in an intraoperative setting.

A. Imaging Setup

The imaging setup is detailed in Fig. 13. The imaging ASIC is shown in Fig. 13(a) on the carrier PCB in the left image. The imaging ASIC with an optical filter attached is shown on the

right. The optical filter is deposited on a fused silica wafer that is diced to fit the imaging ASIC. After deposition, the diced filters are epoxied on the surface of the ASIC using a clear optical epoxy. Dark epoxy is used for electrical isolation. Fig. 13(b) shows the setup for capturing fluorescence microscope images simultaneously with images from the ASIC. The ASIC and carrier PCB (top) are suspended over an inverted fluorescence microscope (bottom). A glass slide carrying the sample to be imaged is held in between the two on an X-Y stage. Fig. 13(c) shows a diagram of this imaging setup. The imaging ASIC and optical filter are shown at the top of the diagram. The fused silica serves as a spacer that separates the imager from the sample to be imaged and has 500 μm thickness.

The sample to be imaged is placed on a 1.5 mm thick glass slide underneath a coverslip that adds 150 μm to the imaging distance. For large tissue samples, a similar procedure is used as shown in Fig. 13(d). An IVIS Spectrum live animal imaging system is used to obtain reference images instead of the fluorescence microscope for these samples due to their large size. The illumination light intensity used for imaging is approximately 7.5 mW and is provided by a collimated laser diode light source. The angle of the excitation light was manually adjusted until the entirety of the 3D cell culture or tissue sample to be imaged was illuminated. This adjustment only occurs once per imaging session, during the initial setup. Afterwards the relative position of the sensor and excitation light remain fixed. For intraoperative use, laser diodes can be placed arrayed around the image sensor in order to illuminate the tissue surface. Care must be taken to make sure the angle required to illuminate the whole surface of the tissue is below the total internal reflection angle (approximately 70°) of the glass-tissue interface at the surface of the spacer placed over the image sensor.

B. 3D Cell Cultures

We have demonstrated imaging with 3D cell cultures in order to characterize the ability of the imager to detect small foci of tumor containing on the order of 200 cells or fewer. These cell cultures used are 40 μm thick, containing approximately 3–4 cell layers. They are labeled using antibodies conjugated to the fluorescent nanoparticle Qdot (quantum dot) 705 (ThermoFisher Scientific). A set of example images is shown in Fig. 14. A long integration time, 1 s, tabletop fluorescence microscope image of the cell sample is shown for reference at the top of the figure. The short integration time, 50 ms, image taken with our ASIC is shown at the bottom of the figure. The image taken with the ASIC is unfiltered and represents the raw data. Despite the lack of post-processing, all of the tumor foci identifiable in the fluorescence microscope image are clearly visible in the ASIC image. The tumor foci labeled A and B contain close to 180 and 270 cancer cells, respectively and are detectable with close to 15 dB SNR.

We can calculate the expected SNR from foci containing 200 cancer cells by combining the fluorescence signal calculations in Section III-C with the pixel responsivity and noise performance as described in Section IV. The expected incident power from 200 cancer cells is 150 fW, the responsivity is 8.2 $\mathrm{Vs}^{-1}\mathrm{pW}^{-1}$, and there is an additional 55% loss due to the presence of the

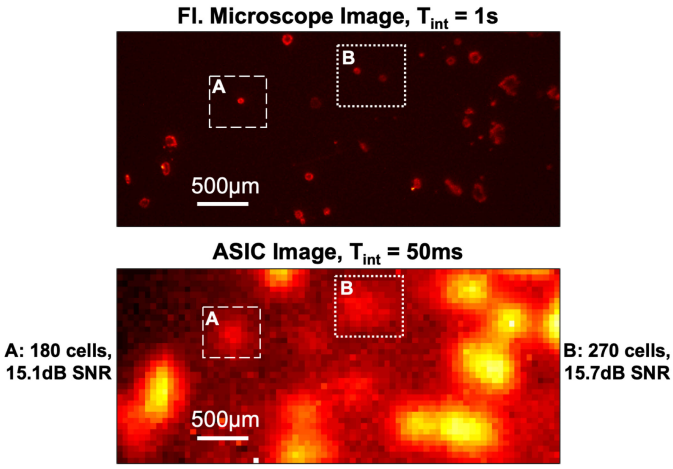

Fig. 14. Example image of 3D cell cultures. A 1 s tabletop fluorescence microscope image is shown (top) for reference and all cancer foci are visible in the 50 ms ASIC image (bottom).

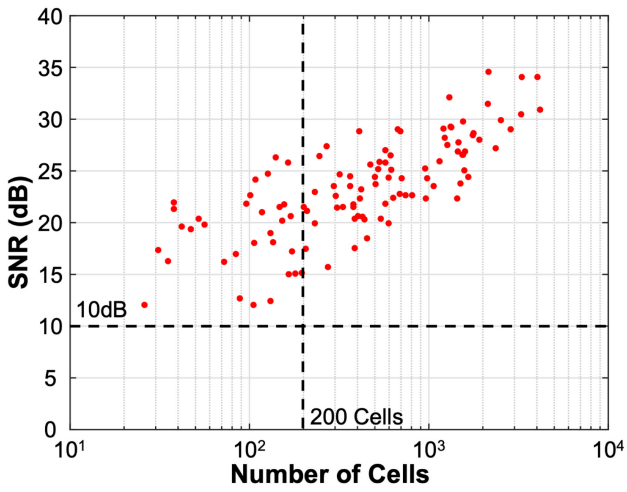

Fig. 15. SNR for tumor foci containing less than one hundred up to thousands of cancer cells.

gratings. For this signal level and an integration time of 50 ms, the expected RMS noise is approximately 4.5 mV, and thus the overall expected SNR is 15.5 dB, very close to the measured results. The signal estimate was conservative, using pessimistic numbers for the total fluorophores per cancer cell. Even higher SNR was measured other foci containing similar numbers of cancer cells, as shown below.

In order to validate the sensor performance for a wide variety of tumor foci sizes, we have imaged over one hundred foci. The SNR versus the number of cells in a focus is plotted in Fig. 15. The plotted SNR represents the SNR of the pixel that received the highest signal from each focus. There is a clear trend with increasing SNR for larger foci, due to their increased signal level. However even for small foci, containing around one hundred cancer cells, the SNR is greater than 10 dB for all cases. There is a spread in the measured SNR for similar sizes due to the morphological difference between these foci (i.e. some foci may be more dense or closely packed than others), variation in the cell size, as well as variation in the binding efficiency of the antibody-fluorophore conjugate.

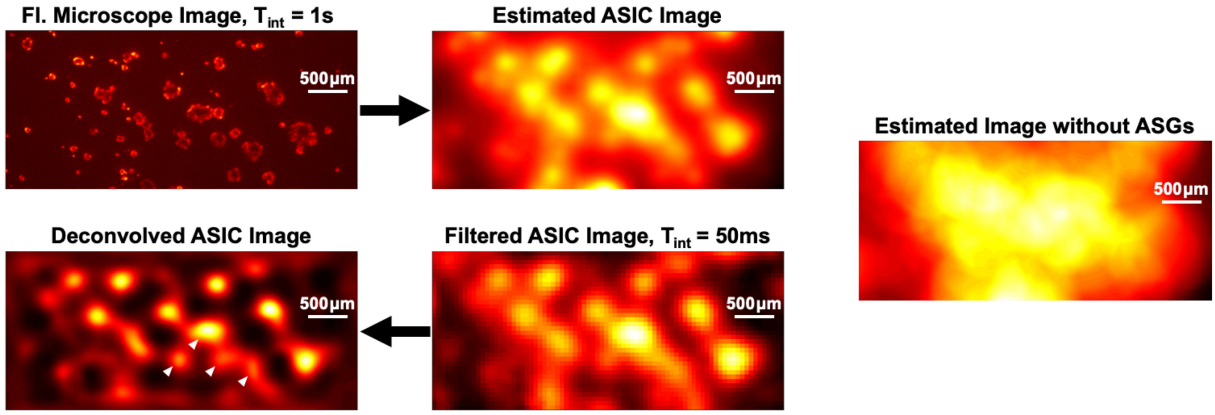

Fig. 16. The PSF predicted using the ASIC angle-selectivity function can be used to estimate the ASIC image (top center) from the captured fluorescence microscope image (top left). Additionally the PSF can be used to deconvolve the images captured using the ASIC (bottom center) in order to obtain a higher resolution image of the tumor (bottom left). The estimated ASIC image and the actual captured image from the ASIC are in very good agreement, indicating that the PSF is predicted correctly. The captured fluorescence microscope image and the deconvolved ASIC image are also in very good agreement. A similar technique can be used to estimate the image that would have been obtained if no ASGs were used in the image sensor (right), thereby illustrating their effectiveness.

To improve the image quality, a variety of computational techniques can be used. As described in Section II-A, the angle-selectivity function can be used to estimate the PSF of the imaging system. The PSF can be used to predict the ASIC images as shown in Fig. 16. The 1 s integration time fluorescence microscope (top left) image is used as the ground truth image and for computing the estimated ASIC image (top center). This image shows very good agreement with a filtered ASIC image (bottom center) taken with a 50 ms integration time. The filtered image is taken using the same process as the image shown on the bottom in Fig. 14 followed by a Gaussian filter with radius equal to the dimension of two pixels on the ASIC (110 μm) to further reduce spatial noise. The PSF of the imaging system is used along with the filtered ASIC image to compute the deconvolved ASIC image (bottom left) using the Lucy-Richardson deconvolution algorithm implemented in software. The resulting images have significantly enhanced resolution compared to the raw chip images. Foci of cancer cells that have blurred together in the filtered image are clearly distinguishable in the deconvolved image (labeled with white arrowheads). This process can provide further information to the surgeon or be used as part of a tumor recognition algorithm to automatically detect if cancer is present based on the captured images.

We can also estimate the images resulting from a contact image sensor that does not use ASGs (applying (1) with an appropriate PSF). Indeed, a photodiode without ASGs has a cosine response with incident angle and, as a result, has a significantly more blurred output image. This is shown on the right side of Fig. 16. Due to the wide angular response of this pixel, the image will change significantly as the imaging distance varies (for example, due to tissue surface topology or a thin liquid layer in the imaging path). Thus deconvolution algorithms are harder to implement and less robust for image sensors that do not incorporate ASGs.

C. Microscopic Residual Mouse Tumor

We have performed imaging of tumor tissue grown in mice (using the procedure described in [12]) in order to demonstrate the ability of the ASIC to detect residual tumor after a resection is completed. The mouse tumor was labeled by performing a systemic injection of the fluorophore IR700DX bound to the antibody Trastuzumab (LI-COR Biosciences) several days before imaging. Fig. 17(a) shows a section of mouse tissue and skin after a breast tumor (with diameter approximately 1 cm) was removed. No tumor is visible and it appears to be normal tissue. However, as shown in Fig. 17(b), an image taken using the IVIS live animal fluorescence imager, two areas of residual tumor remain on the tissue. We imaged the outlined area in Fig. 17(b) using the ASIC and the resulting image is shown in Fig. 17(c). A clear area of residual tumor is visible and outlined in white. A focus of tumor with diameter close to 500 μm is detected with a very high 45 dB SNR and an integration time of only 40 ms. This residual tumor could not have been detected without fluorescence imaging by

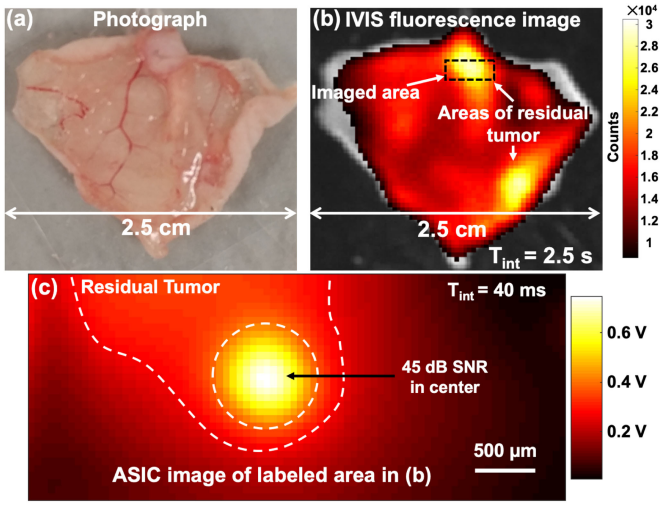

Fig. 17. (a) Photograph of remaining tissue and skin after a large (~1 cm) mouse tumor was removed. No tumor is visible to the naked eye. (b) Image of the same tissue taken with an IVIS fluorescence imager showing two clear areas of residual cancer. (c) Image of the area outlined in (b) taken with the ASIC showing the presence of ~500 μm diameter section of tumor remaining on the tissue.

TABLE I
PERFORMANCE COMPARISON TO OTHER CHIP-SCALE BIOIMAGERS

	2011 [8]	2016 [9]	2009 [10]	2012 [11]	2017 [4]	This work
Detection method	Fluorescence	Fluorescence	Fluorescence	Chemiluminescence	Fluorescence	Fluorescence
Technology	0.18 µm CMOS	Discrete comp.	0.35 µm	0.35 µm	65 nm CMOS	0.18 µm CMOS
For *in vivo* use?	**Yes**	**Yes**	No	No	No	**Yes**
Array size	Single photodiode	6 photodiode clusters	7X8	128X64	Single photodiode	80X36
Pixel size	0.75 mm^2	1 mm^2	250 µmX250 µm	19 µmX19 µm	91.4 µmX123 µm	55 µmX55 µm
Excitation Power	N/A	500 mW*	3 mW	N/A	4 mW	7.5 mW
Imaging Rate	N/A	10 scan/s	N/A	N/A	N/A	20–100 frame/s
Integration time	500 µs	N/A	1 s	1–90 s	0.1–1 s	10–50 ms

*Estimated based on reported laser diode current and datasheet.

eye or touch (the methods currently available to surgeons) after the removal of the large section of tumor.

VI. CONCLUSION

A comparison of the imager presented in this paper to several other chip-scale imagers for biomedical applications appears in Table I. These imagers generally fall into two categories: those that are capable of performing *in vivo* imaging ([8], [9]) and those that have been designed for lab-on-a-chip applications ([4], [10], [11]). The former sensors are only capable of imaging single points or large areas of tumor tissue and do not have sufficient resolution to image microscopic residual cancer consisting of foci containing only hundreds of cancer cells. The latter sensors can be capable of high resolution imaging, but typically require microfluidics or cell/tissue samples to be placed on the ASIC surface, which make them unsuitable for *in vivo* imaging.

We have designed a chip-scale fluorescence imaging ASIC that uses ASGs to enhance image resolution and has the ability to detect small foci containing less than 200 cancer cells. The sensor is capable of capturing high resolution images in real-time and has the ability to be used *in vivo*. We have performed imaging on tumors grown in mice and can detect residual cancer that is undetectable with the naked eye after the main section of tumor is removed, demonstrating the sensor's utility for intraoperative cancer treatment.

APPENDIX
EXTENDED NOISE EQUATIONS

In general, the resistance, R_S, of the switches SW_1 and SW_2 in Fig. 11 should be chosen to not limit the settling time of the amplifier ($R_S \lessapprox \frac{R_{out}}{10}$). However if this is not the case, this switch resistance can potentially affect the noise performance. For the switch noise transfer function, it is simplest to look at the impedance divider formed by the load capacitance, the resistance of each switch, and the parallel combination of all the other impedances connected to the output of the in-pixel amplifier. The last term is Z_1 at the beginning of the integration time and Z_2 at the end of the integration time:

$$Z_1 = R_{out} \left\| \left(\frac{1}{sC_{int}(1-F)} \right) \right\| \left(R_S + \frac{1}{sC_{L1}} \right), \quad (9)$$

$$Z_2 = R_{out} \left\| \left(\frac{1}{sC_{int}(1-F)} \right) \right., \quad (10)$$

For SW_2, the noise transfer function is of the same general form as Eq. (6) and its transfer function (using a series resistor noise voltage as input) at the beginning of integration can be expressed as:

$$H_{n,SW2,1}(s) = \frac{Z_1}{(1+sR_SC_{L,1})\left(Z_1 + R_S + \frac{1}{sC_{L1}}\right)}. \quad (11)$$

The transfer function at the end of integration can be expressed as:

$$H_{n,SW2,2}(s) = \frac{1}{1+sC_{L,2}(R_S+Z_2)}. \quad (12)$$

There is no noise transfer function for SW_1 at the end of integration since the switch is open. Thus the noise from this switch is unaffected by CDS and its overall noise transfer function can be expressed as:

$$H_{n,SW1}(s) = \frac{1}{1+sC_{L,1}(R_S+Z_1)}. \quad (13)$$

The complete transfer functions for thermal, flicker, and shot noise can be found most easily by replacing the C_L terms in the expanded versions of Eq. (7) and Eq. (8) with the term $\frac{C_L}{1+sR_SC_L}$ to account for the different amplifier load impedance and multiplying each equation by $\frac{1}{1+sR_SC_L}$ to account for the low-pass filter behavior of the switch and load capacitance.

ACKNOWLEDGMENT

The authors would like to thank H. Zhang, Dr. C. Park, and Dr. B. Hann (UCSF) for providing 3-D cell culture and tissue samples for imaging. The UCSF Institutional Animal Care and Use Committee (IACUC) approved all experimental procedures involving animal models. The TSMC University Shuttle Program provided CMOS chip fabrication.

REFERENCES

[1] A. Wang, P. R. Gill, and A. Molnar, "An angle-sensitive CMOS imager for single-sensor 3 D photography," in *Proc. IEEE Int. Solid-State Circuits Conf.*, Feb. 2011, pp. 412–414.
[2] S. Sivaramakrishnan, A. Wang, P. Gill, and A. Molnar, "Design and characterization of enhanced angle sensitive pixels," *IEEE Trans. Electron Devices*, vol. 63, no. 1, pp. 113–119, Jan. 2016.
[3] S. Jayasuriya, S. Sivaramakrishnan, E. Chuang, D. Guruaribam, A. Wang, and A. Molnar, "Dual light field and polarization imaging using CMOS diffractive image sensors," *Opt. Lett.*, vol. 40, no. 10, pp. 2433–2436, May 2015.

[4] L. Hong, H. Li, H. Yang, and K. Sengupta, "Fully integrated fluorescence biosensors on-chip employing multi-functional nanoplasmonic optical structures in CMOS," *IEEE J. Solid-State Circuits*, vol. 52, no. 9, pp. 2388–2406, Sep. 2017.
[5] A. E. Giuliano *et al.*, "Breast cancer—Major changes in the American Joint Committee on cancer eighth edition cancer staging manual," *CA, Cancer J. Clin.*, vol. 67, no. 4, pp. 290–303, 2017.
[6] G. M. Van Dam *et al.*, "Intraoperative tumor-specific fluorescence imaging in ovarian cancer by folate receptor-α targeting: First in-human results," *Nature Med.*, vol. 17, no. 10, pp. 1315–1319, Oct. 2011.
[7] D. Shin, M. C. Pierce, A. M. Gillenwater, M. D. Williams, and R. R. Richards-Kortum, "A fiber-optic fluorescence microscope using a consumer-grade digital camera for in vivo cellular imaging," *PLoS One*, vol. 5, no. 6, Jun. 2010, Art. no. e11218.
[8] R. T. Heitz, D. B. Barkin, T. D. O'Sullivan, N. Parashurama, S. S. Gambhir, and B. A. Wooley, "A low noise current readout architecture for fluorescence detection in living subjects," in *Proc. IEEE Int. Solid-State Circuits Conf.*, Feb. 2011, pp. 308–310.
[9] P. Demosthenous, C. Pitris, and J. Georgiou, "Infrared fluorescence-based cancer screening capsule for the small intestine," *IEEE Trans. Biomed. Circuits Syst.*, vol. 10, no. 2, pp. 467–476, Apr. 2016.
[10] B. Jang, P. Cao, A. Chevalier, A. Ellington, and A. Hassibi, "A CMOS fluorescent-based biosensor microarray," in *Proc. IEEE Int. Solid-State Circuits Conf., Dig. Tech. Papers*, Feb. 2009, pp. 436–437,437a.
[11] R. R. Singh, L. Leng, A. Guenther, and R. Genov, "A CMOS-microfluidic chemiluminescence contact imaging microsystem," *IEEE J. Solid-State Circuits*, vol. 47, no. 11, pp. 2822–2833, Nov. 2012.
[12] E. P. Papageorgiou, S. Giverts, H. Zhang, C. Park, B. E. Boser, and M. Anwar, "Imaging of IR700dx labeled mouse breast tumor using a custom angle-selective fluorescence contact imaging system," in *Proc. 40th Annu. Int. Conf. IEEE Eng. Med. Biol. Soc.*, Jul. 2018, pp. 1–4.
[13] M. Koch *et al.*, "Threshold analysis and biodistribution of fluorescently labeled bevacizumab in human breast cancer," *Cancer Res.*, vol. 77, no. 3, pp. 623–631, Feb. 2017.
[14] E. P. Papageorgiou, H. Zhang, B. E. Boser, C. Park, and M. Anwar, "Angle-insensitive amorphous silicon optical filter for fluorescence contact imaging," *Opt. Lett.*, vol. 43, no. 3, pp. 354–357, Feb. 2018.
[15] A. Penzkofer and P. Sperber, "Measurement of absorption cross sections in the long-wavelength region of the S0-S1 absorption band of dyes," *Chem. Phys.*, vol. 88, no. 2, pp. 309–313, Aug. 1984.
[16] L. Wang, A. K. Gaigalas, and V. Reipa, "Optical properties of Alexa 488 and Cy 5 immobilized on a glass surface," *Biotechniques*, vol. 38, no. 1, pp. 127–132, 2005.
[17] G. Hong *et al.*, "Near-infrared-fluorescence-enhanced molecular imaging of live cells on gold substrates," *Angewandte Chemie Int. Ed.*, vol. 50, no. 20, pp. 4644–4648, May 2011.

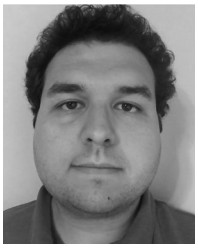

Efthymios P. Papageorgiou (S'15–M'19) received the B.Sc. degree from Columbia University, New York, NY, USA, in 2014 where he worked with Prof. Yannis Tsividis on continuous time hybrid analog-digital circuits, and the Ph.D. degree from the Department of Electrical Engineering and Computer Sciences, University of California, Berkeley, CA, USA, in May 2019. His research at UC Berkeley was focused on biomedical circuits and systems, especially concerning devices for intraoperative cancer detection. He worked at Qualcomm Technologies during the Summer of 2017 on digital power amplifier design. He is currently with the Bosch Research and Technology Center, Sunnyvale, CA, USA. He was the recipient of the Edwin Howard Armstrong Memorial Award from Columbia University in 2014, the Berkeley Fellowship for Graduate Study in 2014, the ADI Outstanding Student Designer Award in 2016, and the NSF Fellowship for Graduate Study in 2016.

Bernhard E. Boser (F'03) received the Ph.D. degree from Stanford University, Stanford, CA, USA, in 1988. He was a Member of Technical Staff at Bell Laboratories. In 1992, he joined the Faculty of the EECS Department, UC Berkeley, Berkeley, CA, USA. He is currently a Co-Founder of SiTime, Santa Clara, CA, USA, and Chirp Microsystems, Berkeley, CA, USA. His current research interests include analog and mixed signal circuits, with special emphasis on ADCs and micromechanical sensors and actuators. He was the President of the Solid-State Circuits Society and on the program committees of ISSCC, VLSI Symposium, and Transducers. He was also the Editor-in-Chief for the IEEE JOURNAL OF SOLID-STATE CIRCUITS.

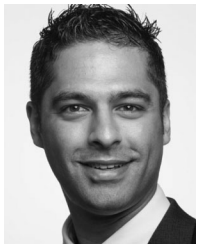

Mekhail Anwar (M'17) received the B.A. degree in physics from UC Berkeley, Berkeley, CA, USA, where he graduated as the University Medalist, and the Ph.D. degree in electrical engineering and computer sciences from the Massachusetts Institute of Technology, Cambridge, MA, USA, in 2007, followed by an MD from the University of California, San Francisco, CA, USA, in 2009. After completing a Radiation Oncology residency in 2014 with UCSF, he joined the faculty with the UCSF Department of Radiation Oncology in 2014. He is board certified in Radiation Oncology and a Core Member of the UC Berkeley and UCSF Bioengineering group. He was the recipient of the Department of Defense Prostate Cancer Research Program Physician Research Award and the NIH Trailblazer Award. His research interests include developing sensors to guide cancer care using integrated-circuit based platforms.